Cronfa - Swansea University Open Access Repository

_____

This is an author produced version of a paper published in :
Materials Chemistry and Physics

_____

Cronfa URL for this paper:
http://cronfa.swan.ac.uk/Record/cronfa31732

_____

Paper:

Claypole, A. Effects of Cd1-xZnxS alloy composition and post-deposition air anneal on ultra-thin CdTe solar cells produced by MOCVD. *Materials Chemistry and Physics*
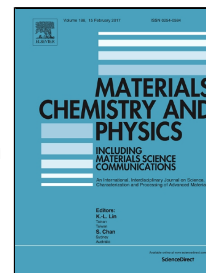http://dx.doi.org/10.1016/j.matchemphys.2017.01.067

_____

Accepted Manuscript

Effects of $Cd_{1-x}Zn_xS$ alloy composition and post-deposition air anneal on ultra-thin CdTe solar cells produced by MOCVD

A.J. Clayton, M.A. Baker, S. Babar, R. Grilli, P.N. Gibson, G. Kartopu, D.A. Lamb, V. Barrioz, S.J.C. Irvine

Effects of $Cd_{1-x}Zn_xS$ alloy composition and post-deposition air anneal on ultra-thin CdTe solar cells produced by MOCVD

A. J. Clayton*[1], M. A. Baker[2], S. Babar[2], R. Grilli[2], P. N. Gibson[3], G. Kartopu[1], D. A. Lamb[1], V. Barrioz[4] and S. J. C. Irvine[1]

[1]Centre for Solar Energy Research, College of Engineering, Swansea University, OpTIC, St. Asaph, LL17 0JD, UK

[2]The Surface Analysis Laboratory, Department of Mechanical Engineering Sciences, University of Surrey, Guildford, GU2 7XH, UK

[3]Institute for Health and Consumer Protection, Joint Research Centre of the European Commission, 21027 Ispra (VA), Italy

[4]Engineering and Environment, Department of Physics and Electrical Engineering, Northumbria University, Newcastle, NE1 8ST, UK

*Corresponding author email: Andrew.J.Clayton@Swansea.ac.uk, +44 1745 535213

Highlights

- $CdCl_2$ anneal treatment resulted in S diffusing to the back contact.

- High Zn levels created mixed cubic/hexagonal structure at the p-n junction.

- Increased Zn in $Cd_{1-x}Zn_xS$ supressed S diffusion into CdTe.

- Device V_{oc} was enhanced overall with an additional back surface air anneal.

Effects of $Cd_{1-x}Zn_xS$ alloy composition and post-deposition air anneal on ultra-thin CdTe solar cells produced by MOCVD

A. J. Clayton*[1], M. A. Baker[2], S. Babar[2], R. Grilli[2], P. N. Gibson[3], G. Kartopu[1], D. A. Lamb[1], V. Barrioz[4] and S. J. C. Irvine[1]

[1]Centre for Solar Energy Research, College of Engineering, Swansea University, OpTIC, St. Asaph, LL17 0JD, UK

[2]The Surface Analysis Laboratory, Department of Mechanical Engineering Sciences, University of Surrey, Guildford, GU2 7XH, UK

[3]Institute for Health and Consumer Protection, Joint Research Centre of the European Commission, 21027 Ispra (VA), Italy

[4]Engineering and Environment, Department of Physics and Electrical Engineering, Northumbria University, Newcastle, NE1 8ST, UK

*Corresponding author email: Andrew.J.Clayton@Swansea.ac.uk, +44 1745 535213

Abstract

Ultra-thin $CdTe:As/Cd_{1-x}Zn_xS$ photovoltaic solar cells with an absorber thickness of 0.5 µm were deposited by metal-organic chemical vapour deposition on indium tin oxide coated boro-aluminosilicate substrates. The Zn precursor concentration was varied to compensate for Zn leaching effects after $CdCl_2$ activation treatment. Analysis of the solar cell composition and structure by X-ray photoelectron spectroscopy depth profiling and X-ray diffraction showed that higher concentrations of Zn in the $Cd_{1-x}Zn_xS$ window layer resulted in suppression of S diffusion across the $CdTe/Cd_{1-x}Zn_xS$ interface after $CdCl_2$ activation treatment. Excessive Zn content in the $Cd_{1-x}Zn_xS$ alloy preserved the spectral response in the blue region of the solar spectrum, but increased series resistance for the solar cells. A modest increase in the Zn content of the $Cd_{1-x}Zn_xS$ alloy together with a post-deposition air anneal resulted in an improved blue response and an enhanced open circuit voltage and fill

factor. This device yielded a mean efficiency of 8.3% over 8 cells (0.25 cm^2 cell area) and best cell efficiency of 8.8%.

1. Introduction

Thin film cadmium telluride (CdTe) has been an established technology for photovoltaic (PV) solar energy for a number of years [1]. Its commercial interest stems from the ease in material synthesis and ideal material properties coupled with high solar cell conversion efficiencies achievable (currently 22.1 % for a cell [2] and 18.6% for a module with aperture area of 7038.8 cm^2 [3]). However, the rate at which Te can be supplied is largely dependent on the mining of Cu and its availability may become limited if the demand of global Te increased significantly [4]. In addition, a decline in the rate of Cu extraction [5] could also impact the Te supply. Reduction of CdTe absorber thickness becomes an important consideration for continued large scale production of CdTe solar modules [6-8]. The use of less material will also have a positive impact for reducing manufacturing costs and carbon footprint providing that the PV conversion efficiency does not deteriorate significantly. However, ultra-thin (≤ 1 μm) CdTe solar cells are more susceptible to lateral inhomogeneity across the device [9, 10] which is a limiting factor for industrial production.

There have been several studies on ultra-thin CdTe PV cells [6, 11-13], reporting a best cell efficiency of 11.2 % for close spaced sublimated (CSS) CdTe cells with an absorber thickness of 0.6 μm [11] and an 11% best and 10% mean efficiency over 25 dot cells (0.06 cm^2 cell area) for 0.5 μm thick CdTe produced by sputtering [13]. These PV cell performances are very respectable when compared to standard CdTe solar devices and absorber thicknesses of 2-5 μm [14, 15]. The power output per mass of material (or tellurium) used (W/g$_{Te}$), which will be referred to as *material*

power yield, increases as the CdTe thickness is reduced. This relates directly to the fact that the majority of carriers are generated close to the junction [9]. The enhanced material power yield with reduced CdTe thickness can be demonstrated considering the reported world record 22.1 % efficiency for a CdTe cell [2]. Assuming a CdTe thickness of 4 µm for this 22.1 % efficient cell, gives a W/g_{Te} of 0.19. For an equivalent 2 µm and 0.5 µm CdTe solar cell using the world record efficiency [2], the W/g_{Te} would be 0.38 and 1.51 respectively. For the reported [13] 11% cell with 0.5 µm CdTe the material power yield is 0.75 W/g_{Te}, which is a significant improvement compared to solar cells with ($\geq$ 2 µm) CdTe thicknesses, even with the current world record efficiency for 2 µm CdTe thickness. This shows the incentive for reducing the CdTe thickness in future commercial production of CdTe modules. This becomes more desirable if there is a sufficient drop in the manufacturing cost from using less material and the deterioration in solar cell/module performances for ultra-thin devices is minimised.

An improved spectral response in the blue region of the solar spectrum has been achieved for ultra-thin CdTe solar cells upon addition of Zn to the CdS layer giving a $Cd_{1-x}Zn_xS$ alloy window layer with a larger band gap [10, 16]. Previous work [17] has shown that metal-organic chemical vapour deposition (MOCVD) can introduce Zn into the CdS window layer in a controlled manner with determination of the optimised levels to give enhanced solar cell performance before the series resistance increases and a change in the lattice structure deteriorates collection at the junction. However, $CdCl_2$ activation treatment was found to reduce the Zn content in the $Cd_{1-x}Zn_xS$ alloy window layer due to Zn leaching [10]. This is significant when the CdTe absorber thickness is reduced. Although the Zn composition in the $Cd_{1-x}Zn_xS$ alloy window layer reduced as the $CdCl_2$ deposition increased, an improvement in open

circuit voltage (V_{oc}) was also observed [18]. This work considers the approach of using higher concentrations of Zn in the $Cd_{1-x}Zn_xS$ alloy window layer to compensate for Zn leaching resulting from $CdCl_2$ activation.

In addition to the improvements in using a $Cd_{1-x}Zn_xS$ alloy window layer, a post-$CdCl_2$ treatment air anneal at low temperature has been found [19, 20] to be beneficial to MOCVD-produced CdTe solar cells. X-ray photoelectron spectroscopy (XPS) has shown [19] that there is oxidation of the CdTe after the air anneal and capacitance-voltage (C-V) measurements have confirmed [20] an increase in acceptor carrier concentration, as well as a reduction in the back contact barrier. These observations were for solar cells with a CdTe absorber thickness of 2.25 μm, but the impact of this treatment on devices with reduced CdTe absorber thickness has not been reported. Other literature report [21, 22] an improved CdTe solar cell performance carrying out the $CdCl_2$ anneal treatment with oxygen present in the chamber.

Changes to the solar cell composition and structure after the same $CdCl_2$ activation treatment are investigated using XPS depth profiling and X-ray diffraction (XRD). Comparison between as-grown and air annealed devices is also made. These results are correlated with the corresponding PV solar cell performance.

2. Experimental

Ultra-thin $Cd_{1-x}Zn_xS$/CdTe solar cells were produced using MOCVD in a single growth chamber. Boro-aluminosilicate glass coated with indium tin oxide was used as the substrate, with a thickness of 1.1 mm and sheet resistance of 4-8 Ω/□. A wide band gap $Cd_{1-x}Zn_xS$ alloy window layer with a thickness of 0.24 µm was employed to enhance the spectral response in the blue region [16-18, 24]. The 0.24 µm window

layer thickness included a 0.05 μm CdS nucleation layer, the first layer to be deposited (at 315°C) in the MOCVD growth chamber on to the ITO, which improved surface coverage of the $Cd_{1-x}Zn_xS$ alloy window layer grown at the higher temperature of 360°C. Interdiffusion of the CdS layer into the $Cd_{1-x}Zn_xS$ alloy occurred during CdTe growth and Cl activation treatment. Different Zn concentrations in the alloy were achieved through varying the Zn precursor partial pressure, P_{Zn}. Arsenic was used as the CdTe acceptor dopant with a mean concentration of ~5 × 10^{18} atoms/cm³, and was introduced into the MOCVD growth chamber during CdTe deposition at 390°C. All devices were treated in the same MOCVD chamber after CdTe growth, with the same $CdCl_2$ activation process; a $CdCl_2$ deposition time of 179 seconds at 200°C and a thermal anneal at 420°C for 10 minutes. The devices being subjected to a post-growth air anneal were placed in an oven at 170 °C for 30 minutes. Details of the processing parameters employed for the different samples are given in Table 1. In this Table, a comparison has been made to an equivalent MOCVD-grown ultra-thin CdTe device receiving no $CdCl_2$ anneal treatment (reference) and a CdTe device with absorber thickness of 2.25 μm (baseline). A previous study [18] determined that a greater $CdCl_2$:CdTe thickness ratio was necessary compare to baseline devices produced using the same method. The approximate $CdCl_2$ thickness has been given, assuming a 1.2 nm/s growth rate determined in previous work [25]. Device PZN07 had a modest increase in the Zn precursor partial pressure (P_{Zn}) than that typically employed (i.e. for the baseline, reference and PZN06 devices) during window layer deposition. For device PZN14, P_{Zn} was raised further, to double that used for device PZN07.

Device	CdTe (μm)	P_{Zn} (atm.)	$CdCl_2$ (s)	$CdCl_2$ (~μm)	Anneal (s)	Air anneal (s)
Baseline	2.25	6.0×10^{-5}	359	431	600	0
Reference	0.5	6.0×10^{-5}	0	0	0	0
PZN06	0.5	6.0×10^{-5}	179	215	600	0
PZN07	0.5	6.9×10^{-5}	179	215	600	30
PZN14	0.5	1.4×10^{-4}	179	215	600	30

Table 1: Ultra-thin $Cd_{1-x}Zn_xS$/CdTe solar cells with variable window layer Zn content controlled using different Zn precursor partial pressures (P_{Zn}) during deposition.

An anneal treatment without $CdCl_2$ was not carried out in this study as the aim of the work was to study the efficiency enhancement associated with Cl^- diffusion in the activation process. After rinsing excess $CdCl_2$ from the surface with deionised water, a further low temperature anneal was carried out for 30 minutes in air using an extracted oven set at 170°C for devices PZN07 and PZN14 prior to back contact formation. Each ultra-thin CdTe solar cell device consisted of 8×0.25 cm^2 cells defined by evaporating Au through a shadow mask. These cells are four times larger in size than other reported [13] high efficiency CdTe solar cells with reduced absorber thickness making them more susceptible to lateral inhomogeneities. The reason for this was to enable comparison to equivalent MOCVD-grown devices with the baseline CdTe absorber thickness. No Cu was added to the Au contacts and no further annealing was carried out, which is typical in CdTe solar cell fabrication to increase p-type activity near the back contact, leading to V_{oc} enhancement. There are still long-term stability concerns [26] when using Cu, which becomes much more significant when considering solar cells with reduced CdTe absorber thickness.

Compositional changes to the ultra-thin $Cd_{1-x}Zn_xS$/CdTe solar cells were investigated using a Thermo Scientific Thetaprobe XPS instrument employing a monochromatic Al K_α X-ray source with an energy of 1486.7 eV. The diameter of the

X-ray beam spot was 800 µm. Wide scan spectra were recorded at a pass energy of 300 eV and narrow scan spectra recorded at pass energy of 20 eV. Quantification of the XPS data was performed after a Shirley background subtraction using the Thermo Scientific Avantage software which employs instrument modified Wagner sensitivity factors. Depth profiling was undertaken using an Ar^+ ion gun operating at 3 keV and current density of 11.1 µA/cm^2 (1 µA induced beam current, rastered over a 3 x 3 mm^2 area). Spectra were charge referenced to the C 1s peak at 285.0 eV.

The $Cd_{1-x}Zn_xS$ XRD peaks were recorded using a Panalytical X'Pert Pro MPD diffractometer employing Cu K_α radiation generated using an accelerating voltage of 40 kV and a current of 30 mA. The diffractograms were acquired in a 2θ range of 15°-75° with a step size of 0.01° and a scan step time of 0.6 seconds. XRD analysis of the CdTe (111) peak was carried out with a Bruker D8 Discover instrument. Copper K_α radiation was used, together with a Lynxeye position sensitive detector. All scans reported here were made in the parafocussing mode due to instrumental resolution being much higher than in the parallel beam mode. Following data collection, the instrument software was used to strip the K_{α_2} component from the diffraction patterns.

Current density – voltage (*J-V*) measurements were carried out with a single pass illumination at air mass (AM)1.5 using an Abet Technologies Ltd. solar simulator employing a light power density output of 100 mW/cm^2 calibrated using a Fraunhofer c-Si reference cell. External quantum efficiency (EQE) measurements were performed using a Bentham spectral response spectrometer under unbiased conditions over the spectral range 0.3 – 1.0 µm.

3. Results and discussion

3.1 XPS

XPS depth profiles were used to examine the Zn concentration in the $Cd_{1-x}Zn_xS$ alloy layer and interdiffusion between the layers following the $CdCl_2$ activation treatment. Figure 1 shows XPS depth profiles for devices PZN06, PZN07 and PZN14. The interface regions are not clearly defined due to individual layer roughness and interdiffusion processes resulting from the activation treatment. However, approximate interface regions have been shown in Figures 1 (a) – (c).
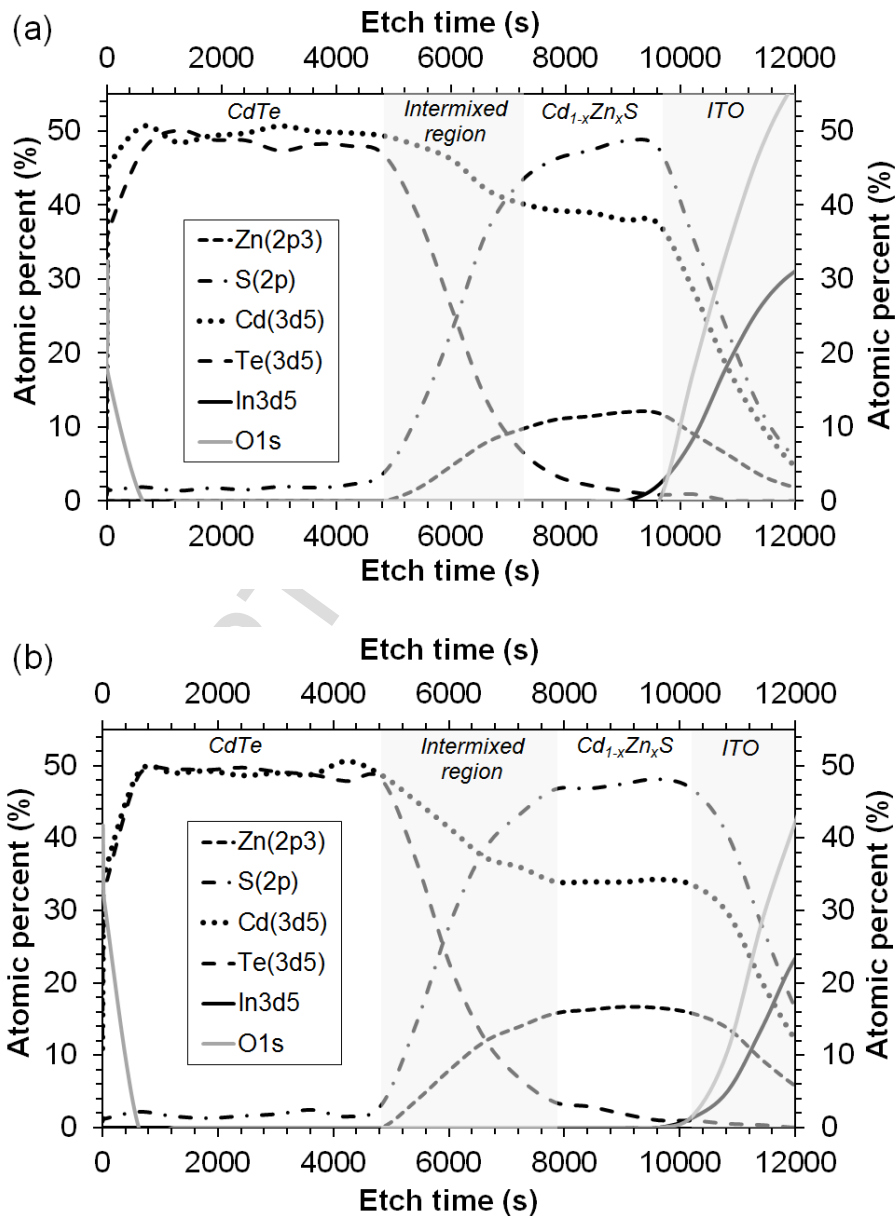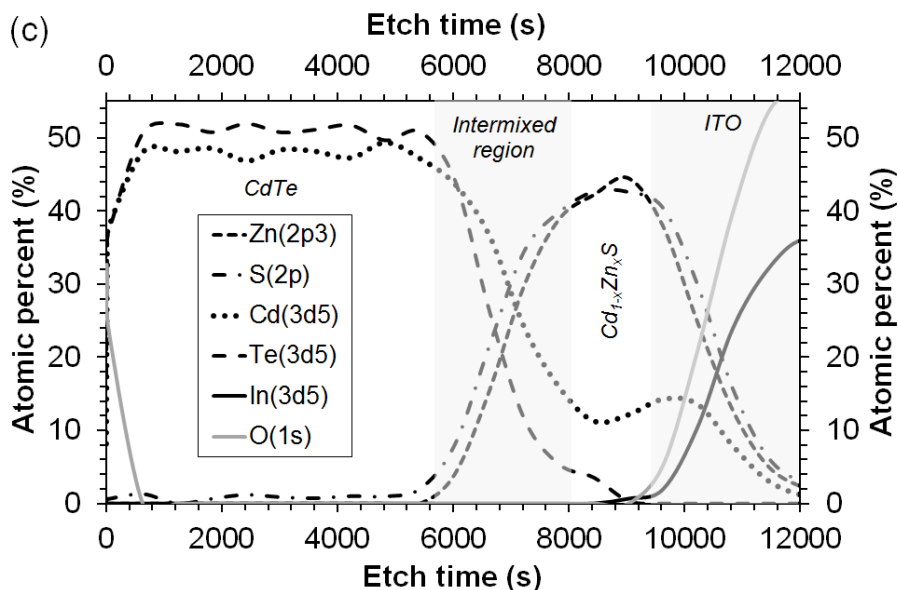
Figure 1: XPS depth profiles for (a) device PZN06, (b) device PZN07 and (c) device PZN14; all having received CdCl$_2$ activation treatment.

Generally, the XPS profile for device PZN06 is similar to that of device PZN07, with the exception that in the Cd$_{1-x}$Zn$_x$S layer the Cd:Zn ratio is higher for PZN06 (3.4), compared to PZN07 (2.1). This is expected considering the 15% increase in concentration of the Zn precursor used for PZN07. This trend is continued for PZN14, where the Cd:Zn ratio decreases substantially to an average value of ~0.3. The progressive increase in Zn content in the window layer results in a corresponding depletion of Cd across the CdTe/Cd$_{1-x}$Zn$_x$S interface as the Zn replaces the Cd, with the gradient across the junction becoming more prominent as the Zn concentration increases in the Cd$_{1-x}$Zn$_x$S layer.

Unlike the behaviour observed for PZN06 and PZN07, where the Cd concentration was relatively uniform within the Cd$_{1-x}$Zn$_x$S layer, for PZN14 shown in Figure 1 (c), there is a clear decrease in Cd concentration approaching the CdTe/Cd$_{1-x}$Zn$_x$S interface. Considering the profiles for Te and Zn, it can be seen that for PZN06, the Te concentration follows a diffusion profile from the CdTe to the

$Cd_{1-x}Zn_xS$ layer, with a typical smooth tailing off of the Te concentration into the $Cd_{1-x}Zn_xS$ layer. However, as the Zn concentration is progressively increased in PZN06 and PZN07, Figure 1 shows there to be a concomitant increase in the Te concentration within the $Cd_{1-x}Zn_xS$ close to the interface with CdTe. This increase in Te concentration would appear to be correlated with the drop in the Cd concentration. The profile for PZN14 also shows a 'shoulder' in an otherwise smoothly rising Zn curve in the region where the Cd concentration drops in the $Cd_{1-x}Zn_xS$ layer. This $Cd_{1-x}Zn_xS$ bilayer, with varying $Cd_{1-x}Zn_xS$ stoichiometries, is a consequence of there being a CdS nucleation layer and high Zn content in the $Cd_{1-x}Zn_xS$ layer [17]. Generally, after $CdCl_2$ treatment, the CdS nucleation layer and $Cd_{1-x}Zn_xS$ alloy interdiffuse into one layer [24], but when excessive Zn is used, a bilayer is formed [17], where interdiffusion after $CdCl_2$ activation treatment results in a pair of $Cd_{1-x}Zn_xS$ layers with different Cd:Zn ratios.

Figure 2 represents the elemental fraction as a bar chart determined by XPS in the window layer region of the devices. All the devices show the diffusion of small amounts of Te into the window layer, which is most probably promoted by the high temperatures used during processing and/or S diffusion into the CdTe layer.

The Zn concentrations for PZN06, PZN07 and PZN14 are those remaining in the device following the $CdCl_2$ activation treatment and loss of Zn from the window layer; the reference device having not received any $CdCl_2$ treatment. Our previous work has shown that the $CdCl_2$ treatment leads to Cl^- ions leaching Zn from the $Cd_{1-x}Zn_xS$ layer [10]. Device PZN06 employed the same P_{Zn} as the reference device (Table 1) and Figure 2 shows that the $CdCl_2$ treatment gives rise to the Zn concentration dropping from 31 at.% to 12 at.% as a result of this treatment. Thus, the Zn content in the alloy layer has dropped by more than 50 % following the $CdCl_2$ treatment.
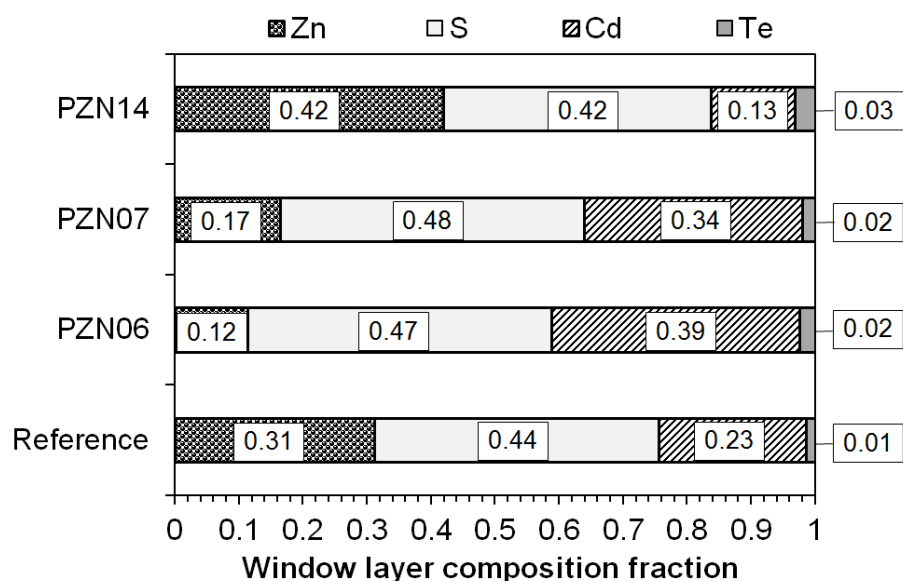
Figure 2: Elemental fraction in the formed quaternary $Cd_{1-x}Zn_xS_{1-y}Te_y$ alloy layer following $CdCl_2$ activation treatment and interdiffusion as determined by XPS.

It has previously been established that the $CdCl_2$ activation treatment leads to S diffusion from the window layer into the CdTe absorber layer [18, 23, 27]. For all of the devices (with the exception of the reference device), S was observed to diffuse through the entire thickness of the CdTe to the back contact (Figure 3). The S concentration throughout the CdTe for PZN14 was determined by XPS to be an average of 1.1 at.% compared to values of 1.7 at.% for PZN07 and 2.0 at.% for PZN06. Figure 3 shows the O and S profiles in the surface region in more detail. As expected, all of the devices exhibit the presence of an oxide at the CdTe surface. It should be noted that the non-air annealed devices (reference and PZN06) were stored under laboratory ambient conditions prior to characterisation by XPS and not kept in an inert atmosphere to protect them from surface oxidation. The two devices thermally annealed in air were examined by XPS and both show much higher oxygen concentrations at the surface, indicative of enhanced surface oxidation resulting from the low temperature anneal in air [19].
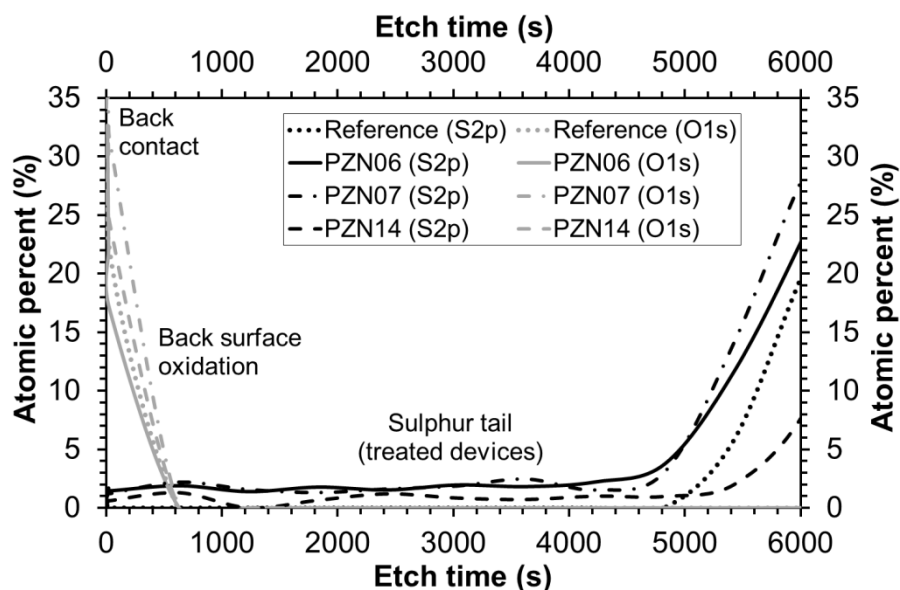
Figure 3: XPS profiles for S(2p) and O(1s) of the reference device with comparison to devices PZN06, PZN07 and PZN14 over the CdTe layer region towards the back contact.

The O concentration drops to zero for all 4 devices after the same Ar$^+$ ion etch time. The surface roughness is dominating this behaviour, which is expected to be similar for all the devices, as observed, due to equivalent growth conditions and CdTe thickness.

3.2 XRD

Figure 4 shows XRD diffractograms for the PZN06, PZN07 and PZN14 devices. The 2θ range between 24.5° and 31.0° is shown, where the main reflections for the hexagonal $Cd_{1-x}Zn_xS$ phase are found. The reference device has been excluded from this Figure due to the presence of only one low intensity diffraction (100) peak for $Cd_{1-x}Zn_xS$ prior to $CdCl_2$ treatment. After treatment and recrystallization, other more prominent diffraction peaks emerge. In Figure 4, a shift of the (100), (002) and (101) $Cd_{1-x}Zn_xS$ peaks by approximately 0.2° to higher angles is observed as the

zinc concentration is increased from 11.5 at.% in PZN06 to 16.5 at.% in PZN07 and again a shift of approximately 0.2° from 16.5 at.% in PZN07 to 41.9 at.% in PZN14. Peak shifts to higher angles, corresponding to a reduction in the lattice parameter, are expected due to the smaller atomic size of Zn compared to Cd. This behaviour was observed in Ref [17] and is clearly shown in the JCPDS patterns for $Cd_{1-x}Zn_xS$ compositions of increasing Zn content, where the $Cd_{1-x}Zn_xS$ stoichiometry progressively changes from CdS to ZnS [28].

Figure 4 shows device PZN06 to have an intense $Cd_{1-x}Zn_xS$ (002) peak and small (101) peak. Device PZN07 has a higher Zn concentration and the diffractogram shows the (100), (002) and (101) reflections exhibiting similar intensities. Device PZN14 contains a much higher Zn content and shows the (002) peak together with a very weak (101) peak. A new peak appears at 28.38°, which can be ascribed to the (111) reflection of the cubic $Cd_{1-x}Zn_xS$ phase. CdS is slightly more stable in the hexagonal form [29, 30] and after $CdCl_2$ treatment and annealing, it usually recrystallizes in the hexagonal phase [31, 32], while ZnS is more stable in the cubic phase at low temperatures [29, 33]. Thus increasing the Zn/Cd ratio to 3.2 is leading to a change in the preferred $Cd_{1-x}Zn_xS$ crystal structure from hexagonal to cubic. There is a shift from strong (002) preferential crystallite growth for PZN06 to more random growth for PZN07 and in PZN14, where there is mixed cubic/hexagonal $Cd_{1-x}Zn_xS$ crystallite growth. The cubic phase is expected to have formed nearer the interface to CdTe, this layer being richer in Zn (Figure 1 c).
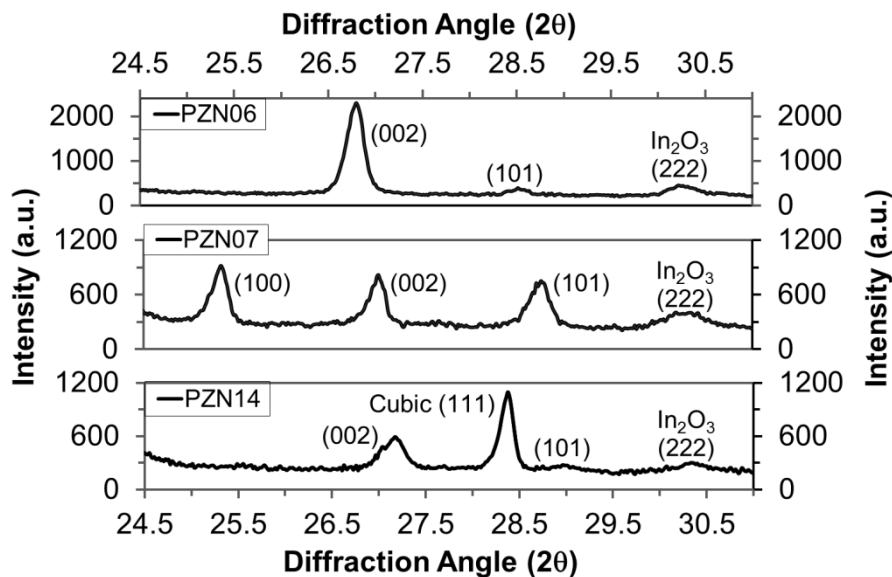
Figure 4: XRD patterns of the $Cd_{1-x}Zn_xS$ window layer in devices PZN06, PZN07 and PZN14 after post-growth $CdCl_2$ treatment; showing hexagonal (100), (002) and (101) orientations for all samples; including a cubic (111) orientation for PZN14 (mixed phase).

S diffusion from $Cd_{1-x}Zn_xS$ into CdTe leads to changes in the XRD diffractograms in the region of the CdTe (111) peak (Figure 5). The as-deposited (reference) film shows a (111) peak position (23.76°) consistent with that expected for bulk CdTe (23.775°) [34]. In contrast, devices which have been $CdCl_2$ treated and air-annealed show a shift in the CdTe peak position to higher angles. This reduction in the lattice parameter arises from the diffusion of S into CdTe. The progressive emergence of a shoulder and then separate peak at higher angles for PZN06, PZN07 and PZN14 corresponds to the formation of a separate $CdTe_{1-y}S_y$ alloy. We have previously shown [27] the increase in intensity of this peak as a function of S concentration diffusing into the CdTe layer following heat treatment and other authors [35] have

also assigned this second peak to the formation of a $CdTe_{1-y}S_y$ solid solution promoted through $CdCl_2$ activation.
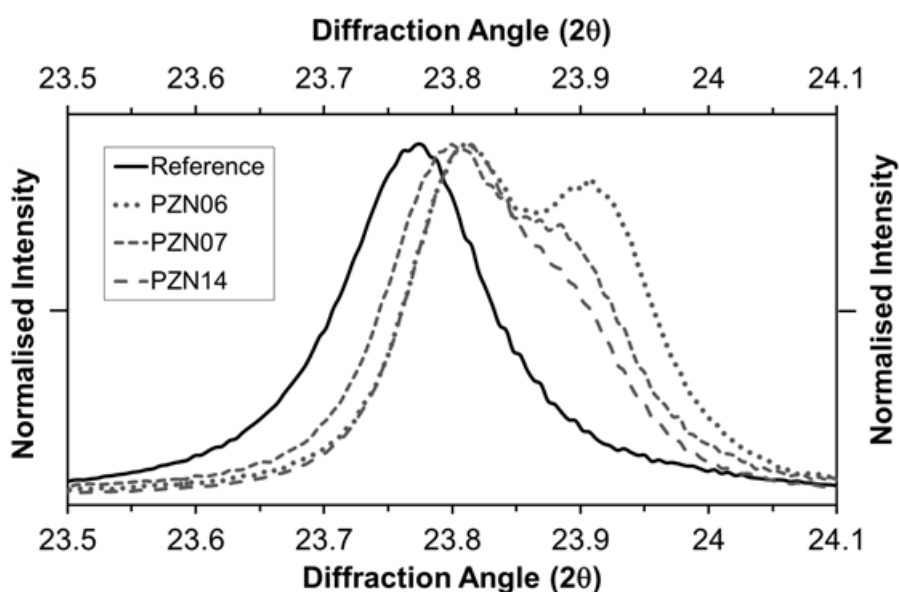
Figure 5: XRD diffraction peaks of the CdTe (111) crystal plane showing variable $CdTe_{1-y}S_y$ phase formation for ultra-thin PV cells with different $Cd_{1-x}Zn_xS$ window layer Zn concentrations.

As the CdTe peaks in Figure 5 have been normalised to the same value and the peak FWHMs of the CdTe are similar, the increased intensity of the $CdTe_{1-y}S_y$ peak compared to the CdTe peak represents an increase in the $CdTe_{1-y}S_y$ phase fraction within the CdTe layer. It can be seen from Figure 5 that the highest peak intensity occurs for PZN06 and lowest intensity for PZN14. This is consistent with the XPS results which showed the highest S concentration in the CdTe layer for PZN06. Hence, excessive Zn content in the $Cd_{1-x}Zn_xS$ alloy window layer acts to supress the degree of S diffusion into the CdTe layer and $CdTe_{1-y}S_y$ phase formation, possibly due to competitive mass transport along the grain boundaries.

3.3 Spectral response

The EQE spectra from the 3 different P_{Zn} devices together with that of the reference device are presented in Figure 6. The EQE spectrum for the ultra-thin reference device that had no $CdCl_2$ activation treatment is also shown for comparison.
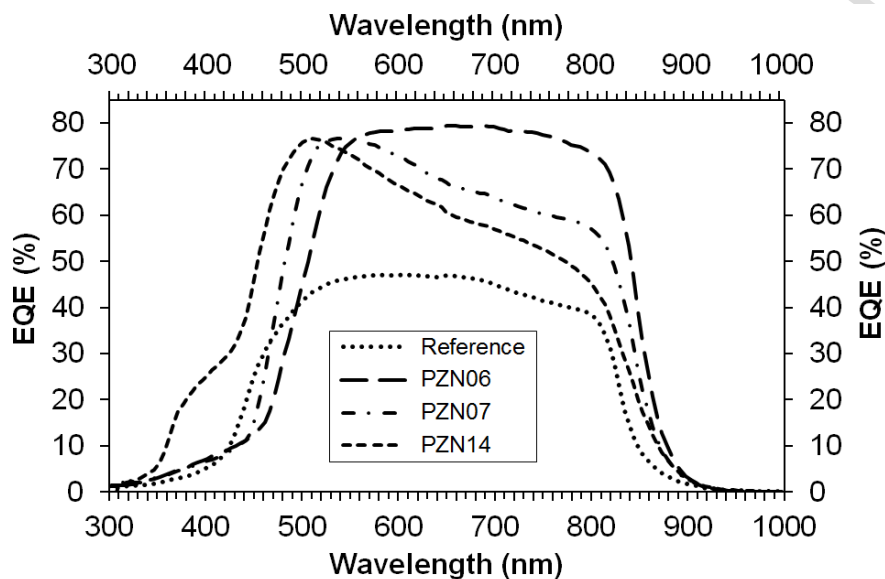
Figure 6: EQE spectra of selected cells from ultra-thin CdTe solar cell devices with different levels of Zn content in $Cd_{1-x}Zn_xS$ and subjected to the same $CdCl_2$ activation treatment.

The EQE spectrum for device PZN14 shows the best spectral blue response for the ultra-thin CdTe solar cells. This correlates well with the high Zn content in the $Cd_{1-x}Zn_xS$ alloy for this device, widening the window layer band gap (E_g). The double absorption edge at the shorter spectral wavelengths is caused by the bilayer of varying $Cd_{1-x}Zn_xS$ layer stoichiometries in the window layer, as shown by the XPS results and discussed in section 3.1.

Figure 6 shows that a modest increase in $Cd_{1-x}Zn_xS$ window alloy Zn content for device PZN07 has still produced an improved spectral response in the blue region of

the solar spectrum (450-500 nm) relative to device PZN06. The window layer absorption edge is red-shifted in comparison to the reference device which received no CdCl$_2$ activation treatment. This is in agreement with it exhibiting a lower Zn content than that in the reference device (Figure 2) and indicates once again the substantial leaching effect of the CdCl$_2$ treatment on the final Zn content within the layer. The CdTe band edge differs for the reference device compared to the other devices that were all treated with CdCl$_2$, which is due to the formation of CdTe$_{1-y}$S$_y$ (Figure 3) for the treated devices as a result of S interdiffusion, leading to a change in the absorber band gap.

Another observation from the EQE results is the significant variation in photocurrent generated over the red region of the solar spectrum. This correlates with the level of Zn incorporation into the Cd$_{1-x}$Zn$_x$S layer where the EQE over the red region falls for devices with progressively higher Zn concentrations. In addition to this, the low temperature air anneal (for devices PZN07 and PZN14) results in a decreasing EQE towards the CdTe band edge, whereas the EQE for device PZN06 (no air anneal) has a fairly flat profile in this spectral region. Ultra-thin CdTe solar cells have been reported [6, 36] to show a decrease in EQE towards the CdTe band edge due to the absorber thickness being insufficient to capture low energy photons at longer wavelengths. Gupta *et al*. [6] reported that ultra-thin cells with Cu/Au back contacts, annealed at 150°C in air promote Cu diffusion into the CdTe layer close to the back contact. EQE simulations by Amin *et al*. [36] showed an increased loss in generated photocurrent at longer wavelengths towards the CdTe band edge as absorber thickness was reduced from 5 down to 0.25 µm. However, the EQE of experimental ultra-thin devices with only Au as the back contact and no air anneal treatment have shown a similar shape in EQE curve to device PZN06 [10]. No

decrease in EQE curve towards the CdTe band edge was observed, even though the CdTe thickness was 0.5 μm (the same as for devices PZN07 and PZN14). It was deduced by the authors that the decreasing slope in the EQE curves towards the CdTe band edge may show a reduced minority carrier lifetime for air annealed ultra-thin cells. The thermal anneal in air increases carrier concentration [20] but consequently depletes the collection depth with increased recombination for carriers generated deeper into the absorber further from the junction.

The energy gap (E_g) of different $Cd_{1-x}Zn_xS$ compositions has been calculated in a previous report [17] using the relationship of absorption coefficient x energy squared versus energy, $(\alpha E)^2$ vs. E, derived from transmittance measurements of single as-grown $Cd_{1-x}Zn_xS$ layers. A comparison was made to the relationship in Equation (1) [37], with a bowing parameter equal to 0.91 and E_g for CdS and ZnS of 2.42 eV and 3.54 eV respectively.

$$E_g(x) = E_g(CdS) + \left[E_g(ZnS) - E_g(CdS) - b\right]x + bx^2 \qquad (1)$$

Figure 7 shows the E_g for $Cd_{1-x}Zn_xS$ versus Zn fraction (x) using the relationship in Equation (1) [37] and the determined E_g values from Kartopu *et al*. [17] for as-deposited (no Cl or air anneal treatment) $Cd_{1-x}Zn_xS$ layers. The ultra-thin devices reported in the current study used similar $Cd_{1-x}Zn_xS$ deposition parameters to Kartopu *et al*. [17], but were incorporated into a complete CdTe device structure with post-growth $CdCl_2$ treatment. These have been included in Figure 7, using the measured Zn fraction from XPS and approximating the E_g from the EQE short wavelength cut-off (window layer absorption edge) in Figure 6.
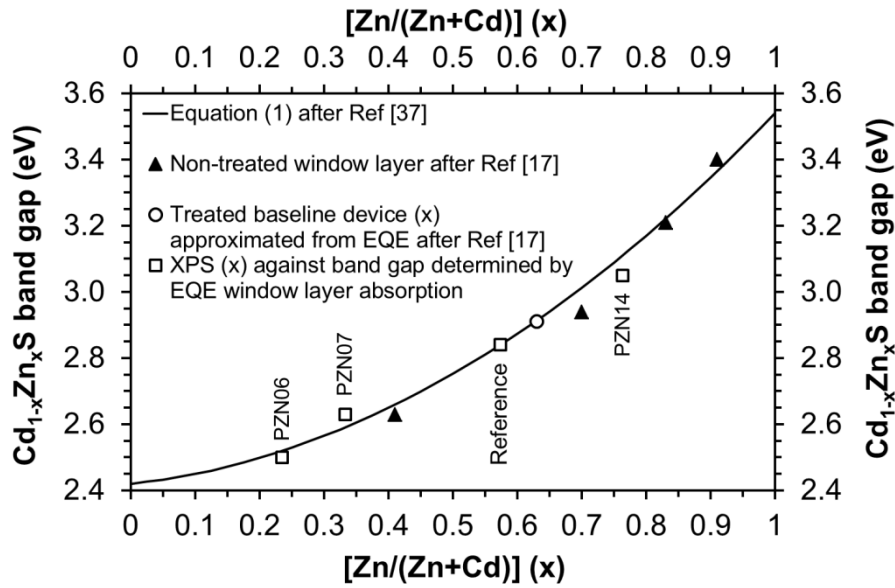
Figure 7: Approximated $Cd_{1-x}Zn_xS$ E_g from EQE short wavelength cut-off (Figure 6) for the reference device, PZN06, PZN07 and PZN14 with the [Zn/(Zn+Cd)] (x) fraction value determined from XPS (open squares); approximated $Cd_{1-x}Zn_xS$ E_g from EQE short wavelength cut-off for a treated baseline device (open circle) after Ref [17]; comparison to non-treated single layer $Cd_{1-x}Zn_xS$ E_g (filled triangles) determined from $(\alpha E)^2$ vs. E [17] and E_g (x) curve from Equation (1) [37].

The E_g determined from the EQE short wavelength cut-off correlated closely to the curve from Equation (1) for the reference device and devices PZN06 and PZN07. An as-grown $Cd_{1-x}Zn_xS$ layer Zn fraction of 0.7 was previously determined [17] to be optimum for device efficiency. The reference device in the current study has a lower Zn fraction than the optimum value, which means that either PZN06 had insufficient Zn concentration prior to $CdCl_2$ treatment. The initial Zn fraction for PZN07 reflected that used for baseline devices reported in Ref [17]. The XPS determined Zn fraction for PZN14 did not show the variation in Zn fraction through the $Cd_{1-x}Zn_xS$ window to be as pronounced across the bi-layer as suggested from the EQE double absorption edge for this device. Interface roughness gives rise to the bilayers being less well-

defined and an 'apparent intermixing' of the two layers, as seen in sputter profiles of other bilayer based structures where intermixing or interface roughness is apparent [38]. Thus the difference in the Cd:Zn ratio for each of the bilayers in the window layer of PZN14 (Figure 6) is greater than that observed in the XPS profile (Figure 1 c). Therefore, an average Zn fraction value for x [Zn/(Zn+Cd)] has been used and the mid-point of the double window layer absorption edge from Figure 6 employed to approximate E_g. An approximation of E_g has also been made using the EQE from a baseline device reported in Ref [17], with the value for x [Zn/(Zn+Cd)] being calculated from Equation 1. What is apparent from Figure 7 is that the level to which Zn is leached out of the $Cd_{1-x}Zn_xS$ window layer is greater for the ultra-thin devices relative to a baseline device taken from Ref [17]. The difference of Zn fraction in the $Cd_{1-x}Zn_xS$ window layer has been tabulated below comparing the initial Zn fraction prior to $CdCl_2$ treatment and the Zn fraction in a device structure post-$CdCl_2$ treatment.

Device	[Zn/(Cd+Zn)] no $CdCl_2$	[Zn/(Cd+Zn)] $CdCl_2$	Zn fraction (x) leached out
Baseline	0.7	0.6	0.1
PZN06	0.6	0.2	0.4
PZN07	0.7	0.3	0.4

Table 2: $Cd_{1-x}Zn_xS$ window layer Zn fractions [Zn/(Zn+Cd)] (x) for equivalent non-$CdCl_2$ treated and post-$CdCl_2$ devices, determining the level of Zn leached out of the device after treatment.

It was reported [17] that device performance deteriorated for $Cd_{1-x}Zn_xS$ window layer initial Zn fraction (x) > 0.7 due to rise in series resistance (R_s) and hence fall in fill factor (*FF*). Figure 7 and Table 2 show that the post-$CdCl_2$ treatment Zn fraction is equal to 0.6. Device PZN14 is above this optimum level (open circle in Figure 7) for

Zn in the $Cd_{1-x}Zn_xS$ window layer. The Zn precursor partial pressure during the MOCVD process to produce device PZN14 was twice the level of that used for device PZN07. Table 2 shows that the level of Zn leached out of a device depends on the absorber thickness and that it should be the same for devices with the same CdTe thickness. This is confirmed in Figure 8, which shows the post-$CdCl_2$ treated Zn fraction (x) determined by XPS against the Zn precursor partial pressure used in the MOCVD process. The optimum Zn fraction x = 0.6 for $Cd_{1-x}Zn_xS$ in a post-$CdCl_2$ treated CdTe device as determined in Ref [17] gives an ideal Zn precursor partial pressure of 1.1×10^{-4} atm. (PZN11) for the MOCVD process, accounting for a Zn fraction loss of 0.4 for an ultra-thin device with CdTe thickness of 0.5 μm.
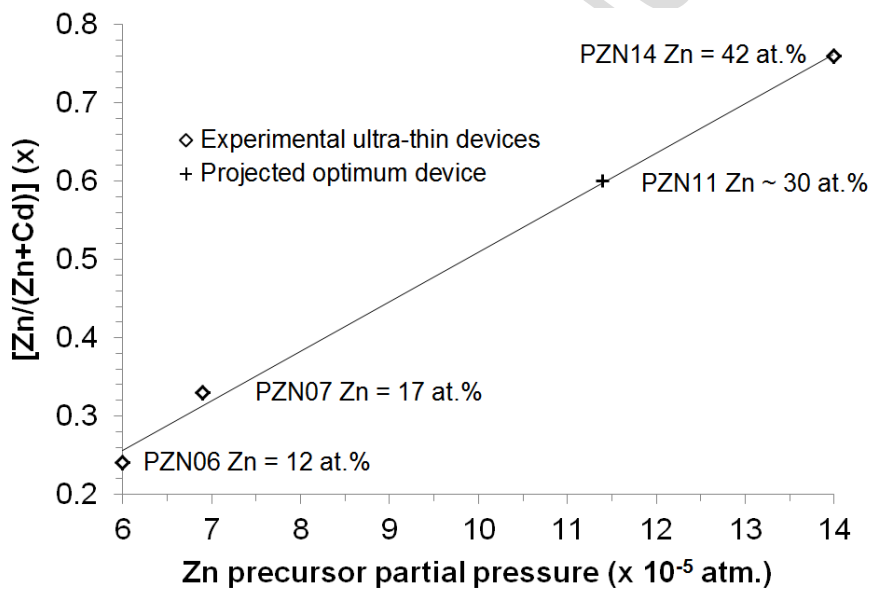

Figure 8: The post-$CdCl_2$ Zn concentration (determined by XPS) as a function of Zn precursor *partial pressure used in the MOCVD process to produce the $Cd_{1-x}Zn_xS$ window layer, showing projected Zn precursor partial pressure required to produce an ultra-thin device with [Zn/(Zn+Cd)] (x) fraction value = 0.6 for the $Cd_{1-x}Zn_xS$ window layer.*

J-V

Table 3 shows the mean *J-V* parameters measured over 8 × 0.25 cm^2 cells from each device and the various treatments given to each device. With regard to V_{oc}, it has been shown previously by the authors [18, 23] that increased S diffusion into the ultra-thin CdTe layer leads to an enhancement in V_{oc}. As mentioned earlier, the amount of S incorporated in the CdTe layer was observed to be 1.1, 1.7 and 2.0 at.% for PZN14, PZN07 and PZN06 respectively. S diffusion into the CdTe layer leads to the formation of a CdTe$_{1-y}$S$_y$ alloy and higher levels of S in the layer results in more CdTe$_{1-y}$S$_y$ being formed (Figure 3). However, Table 2 shows that the device exhibiting the highest S diffusion, PZN06, does not exhibit the highest V_{oc}.

Device	Treatment	Best η (%)	Mean η (%)	J_{sc} (mA/cm^2)	V_{oc} (mV)	FF (%)	R_s (Ω cm^2)	R_{sh} (Ω cm^2)
Reference	as-grown	2.7	2.6 ± 0.2	11.0 ± 0.7	483 ± 7.1	47.9 ± 4.2	10.5 ± 2.5	218 ± 49
PZN06	CdCl$_2$ anneal only	7.1	6.8 ± 0.5	19.4 ± 0.4	584 ± 7.1	60.1 ± 4.0	3.0 ± 0.2	515 ± 100
PZN07	CdCl$_2$ + air anneal	8.8	8.3 ± 0.5	18.4 ± 1.0	644 ± 7.1	69.8 ± 0.5	3.0 ± 0.4	658 ± 164
PZN14	CdCl$_2$ + air anneal	6.1	5.8 ± 0.3	17.4 ± 0.9	591 ± 9.3	56.1 ± 1.5	8.1 ± 0.5	474 ± 119

Table 3: Mean J-V parameters with standard deviation for each ultra-thin CdTe device consisting of 8 × 0.25 cm^2 cells showing different thermal anneal treatments.

It has been demonstrated [19] that for solar cell devices with a CdTe thickness of 2.25 µm (baseline) produced by MOCVD in a hydrogen atmosphere, annealing the device in air after the CdCl$_2$ treatment also leads to an increase in V_{oc}. Capacitance measurements [20] of as-grown and air annealed devices have shown that the carrier concentration in bulk CdTe increases for the air annealed devices. Both devices PZN07 and PZN14 were subjected to the same low temperature air anneal (170 °C for 30 minutes), prior to gold metallisation for back contact formation. These two air annealed devices show the highest values of V_{oc} (Table 3), with PZN07 clearly exhibiting the largest V_{oc}. The reduced V_{oc} for device PZN14 compared to

PZN07 is associated with a lower S concentration in the CdTe, but an additional effect is probably the mixed hexagonal/cubic structure in the window layer, causing more defects in the p-n junction region. As previously discussed, the EQE of the devices annealed in air (Figure 6) show a drop in photocurrent generation at the red wavelengths, which continues towards the CdTe band edge. This explains why the J_{sc} decreases despite a blue shift in the short wavelength response with increasing Zn concentration.

It is also evident from Table 3 that an increase in R_s has occurred for PZN14, lowering the FF and this is caused by the high Zn concentration in the $Cd_{1-x}Zn_xS$ window layer [39]. This has also been shown [17] for equivalent CdTe PV devices with a baseline absorber thicknesses of 2.25 µm. The poor R_s for the reference device can be attributed to the absence of any $CdCl_2$ activation treatment. For device PZN07, which had a lower Zn concentration in the $Cd_{1-x}Zn_xS$ window, the oxidation at the back surface has improved the shunt resistance (R_{sh}), contributing to a boost in FF. This combined with enhanced V_{oc} from the air anneal gives mean cell efficiencies of 8.3 % over 8 × 0.25 cm^2 cells with the best cell efficiency of 8.8 % for a solar cell with CdTe thickness of 0.5 µm. Optimisation of the Zn concentration in the $Cd_{1-x}Zn_xS$ window layer to achieve a Zn concentration of ~ 30% and Zn fraction [Zn/(Zn+Cd)] (x) = 0.6 post-$CdCl_2$ treatment, as projected in Figure 8, should lead to further improvement in performance.

The material power yield was calculated for this ultra-thin cell giving a value of 0.6 W/g_{Te}. A current high efficiency 16.1% CdTe solar cell, produced using an equivalent MOCVD process, with standard 2.25 µm absorber thickness [20], has a material power yield of 0.24 W/g_{Te}. If the gap between the PV performance of ultra-thin cells and equivalent cells with thicker CdTe can be narrowed, the cost of producing

commercial CdTe PV modules may become more attractive, with the issue of increasing Te demand being less of a concern if the absorber thickness was ultra-thin.

4. Conclusions

Three ultra-thin $Cd_{1-x}Zn_xS$/CdTe devices with different Zn concentrations were produced and treated with the same $CdCl_2$ treatment. Two of the cells were given an additional low temperature air anneal. Increased concentrations of Zn in $Cd_{1-x}Zn_xS$ compensated for the leaching of Zn from the device during $CdCl_2$ activation treatment and preserved the spectral response in the blue region of the solar spectrum. However, this corresponded with an overall decrease in EQE over the red region and decrease in the generated photocurrent for devices with increased Zn content in $Cd_{1-x}Zn_xS$.

Increasing the Zn concentration in the $Cd_{1-x}Zn_xS$ alloy suppresses S diffusion into the CdTe layer and leads to the formation of cubic $Cd_{1-x}Zn_xS$ phase in addition to the normal hexagonal phase. The mixed cubic/hexagonal structure increases disorder at the p-n junction interface and contributes to a greater density of defects. In the CdTe layer, a higher concentration of S diffusion leads to a greater fraction of $CdTe_{1-y}S_y$ alloy being formed. The lower fraction of $CdTe_{1-y}S_y$ formed and higher defect density lead to a lower V_{oc} for the cell with a high Zn containing $Cd_{1-x}Zn_xS$ layer.

The additional air anneal prior to back contact metallisation also contributed to V_{oc} improvement, as well as increasing FF for PZN07 by improving R_{sh}. However, excessive Zn incorporation into the $Cd_{1-x}Zn_xS$ layer, forming a ZnS like cubic structure, contributed to a significant increase in R_s causing a drop in FF for PZN14. A modest increase in Zn content in the $Cd_{1-x}Zn_xS$ was required to improve the blue

response without deterioration of *FF* for PZN07. Although this moderate increase in Zn still supressed $CdTe_{1-y}S_y$ alloy formation to some degree, V_{oc} was enhanced overall with the additional back surface air anneal. This resulted in PZN07 having the most improved solar cell performance of the ultra-thin devices, with a mean efficiency of 8.3% over 8 cells (cell areas of 0.25 cm^2) and best cell efficiency of 8.8%. Previous work has shown that an ideal post-$CdCl_2$ treated Zn fraction [Zn/(Zn+Cd)] of x = 0.6 is required for the $Cd_{1-x}Zn_xS$ window layer in the MOCVD-grown CdTe devices. This shows that the ultra-thin device performance can be improved upon, with a device produced with Zn precursor partial pressure of 1.1×10^{-4} atm. (PZN11) likely to give optimised solar cell efficiencies.

Ultra-thin CdTe solar cells have been shown to have a significantly greater W/g_{Te} compared to equivalent devices with thicker CdTe absorber layers, with a value of 0.6 W/gTe for the 8.8 % ultra-thin cell with CdTe thickness 0.5 μm compared to 0.24 W/gTe for an equivalent MOCVD-CdTe cell with baseline thickness 2.25 μm and 0.38 W/gTe for the world record 22.1 % cell assuming 2 μm CdTe thickness. This may become an important consideration with further demand on the global Te supply.

Acknowledgements

References

1. A. Bosio, D. Menossi, S. Mazzamuto and N. Romeo, Manufacturing of CdTe thin film photovoltaic modules, Thin Solid Films 519 (2011) 7522 – 7525.

2. http://investor.firstsolar.com/releasedetail.cfm?ReleaseID=956479 , "First Solar Achieves Yet Another Cell Conversion Efficiency World Record", Durability Milestones, release detail 23rd February 2016, accessed 26th April 2016

3. M. A. Green, K. Emery, Y. Hishikawa, W. Warta and E. D. Dunlop, Solar cell efficiency tables (Version 47), Prog. Photovolt. Res. Appl. 24 (2016) 3 - 11.

4. M. L. Bustamante and G. Gaustad, Challenges in assessment of clean energy supply-chains based on byproduct minerals: A case study of tellurium use in this film photovoltaics, Appl. Energy 123 (2014) 397 – 414.

5. H. U. Sverdrup, K. V. Ragnarsdottir and D. Koca, On modelling the global copper mining rates, market supply, copper price and the end of copper reserves, Resour. Conserv. Recycl. 87 (2014) 158 – 174.

6. A. Gupta, V. Parikh and A. D. Compaan, High efficiency ultra-thin sputtered CdTe solar cells, Sol. Energy Mater. Sol. Cells 90 (2006) 2263 – 2271.

7. C. Candelise, J. F. Speirs and R. J. K. Gross, Materials availability for thin film (TF) PV technologies development: a real concern?, Renew. Sus. Energy Rev. 15 (2012) 4972 – 4981.

8. A. Salavei, I. Rimmaudo, F. Piccinelli and A. Romeo, Influence of CdTe thickness on structural and electrical properties of CdTe/CdS solar cells, Thin Solid Films 535 (2013) 257 - 260.

9. S. J. C. Irvine, V. Barrioz, A. Stafford and K. Durose, Materials issues for very thin film CdTe for photovoltaics, Thin Solid Films 480-481 (2005) 76 - 81.

10. A. J. Clayton, S. J. C. Irvine, E. W. Jones, G. Kartopu, V. Barrioz and W. S. M. Brooks, MOCVD of $Cd_{(1-x)}Zn_{(x)}S$/CdTe PV cells using an ultra-thin absorber layer, Sol. Energy Mater. Sol. Cells 101 (2012) 68 - 72.

11. N. Amin, T. Isaka, A. Yamada, M. Konagai, Highly efficient 1 µm thick CdTe solar cells with textured TCOs, Sol. Energy Mater. Sol. Cells 67 (2001) 195 - 201.

12. V. Plotnikov, X. Liu, N. Paudel, D. Kwon, K. A. Wieland, A. D. Compaan, Thin-film CdTe cells: reducing the CdTe, Thin Solid Films 519 (2011) 7134 – 7137.

13. N. R. Paudel, K. A. Wieland, A. D. Compaan, Ultrathin CdS/CdTe solar cells by sputtering, Sol. Energy Mater. Sol. Cells 105 (2012) 109 – 112.

14. S. J. C. Irvine, V. Barrioz, D. Lamb, E. W. Jones and R. L. Rowlands-Jones, MOCVD of thin film photovoltaic solar cells — next-generation production technology?, J. Cryst. Growth 310 (2008) 5198-5203.

15. W. L. Rance, J. M. Burst, D. M. Meysing, C. A. Wolden, M. O. Reese, T. A. Gessert, W. K. Metzger, S. Garner, P. Cimo and T. M. Barnes, 14%-efficient flexible CdTe solar cells on ultra-thin glass substrates, Appl. Phys. Lett. 104 (2014) 1439031 – 1439034.

16. E. W. Jones, V. Barrioz, S. J. C. Irvine and D. Lamb, Towards ultra-thin CdTe solar cells using MOCVD, Thin Solid Films 517 (2009) 2226-2230.

17. G. Kartopu, A. J. Clayton, W. S. M. Brooks, S. D. Hodgson, V. Barrioz, A. Maertens, D. A. Lamb and S. J. C. Irvine, Effect of window layer composition in Cd1−xZnxS/CdTe solar cells, Prog. Photovolt. Res. Appl. 22 (2014) 18-23.

18. A. J. Clayton, M. A. Baker, S. Babar, P. N. Gibson, S. J. C. Irvine, G. Kartopu, D. A. Lamb and V. Barrioz, Influence of $CdCl_2$ activation treatment on ultra-thin $Cd_{1-x}Zn_xS$ /CdTe solar cells, Thin Solid Films 590 (2015) 241-247.

19. S. L. Rugen-Hankey, A. J. Clayton, V. Barrioz, G. Kartopu, S. J. C. Irvine, J. D. McGettrick and D. Hammond, Improvement to thin film CdTe solar cells with controlled back surface oxidation, Sol. Energy Mater. Sol. Cells 136 (2015) 213 - 217.

20. G. Kartopu, L. J. Phillips, V. Barrioz, S. J. C. Irvine, S. D. Hodgson, E. Tejedor, D. Dupin, A. J. Clayton, S. L. Rugen-Hankey, and K. Durose, Progression of metal-organic vapour-deposited CdTe thin-film PV devices towards modules, Prog. Photovolt. Res. Appl. 24 (2016) 283-291.

21. K. Durose, M. A. Cousins, D. S. Boyle, J. Beier and D. Bonnet, Grain boundaries and impurities in CdTe/CdS solar cells, Thin Solid Films, 403–404 (2002) 396-404.

22. S. Vatavu, H. Zhao, V. Padma, R. Rudaraju, D. L. Morel, P. Gaşin, I. Caraman and C. S. Ferekides, Photoluminescence studies of CdTe films and junctions, Thin Solid Films 515 (2007) 6107-6111.

23. A. J. Clayton, S. Babar, M. A. Baker, G. Kartopu, D, A, Lamb, V. Barrioz and S. J. C. Irvine, Effects of $CdCl_2$ treatment on ultra-thin MOCVD-CdTe solar cells, 28th Euro. Photovolt. Sol. Energy Conf. Proc., Paris, 2013, 3AO6.5.

24. G. Kartopu, A. A. Taylor, A. J. Clayton, V. Barrioz, D. A. Lamb and S. J. C. Irvine, $CdCl_2$ treatment related diffusion phenomena in $Cd_{1-x}Zn_xS$/CdTe solar cells, J. Appl. Phys. 115 (2014) 1045051 - 1045055.

25. V. Barrioz, S. J. C. Irvine, E. W. Jones, R. L. Rowlands and D. A. Lamb, *In situ* deposition of cadmium chloride films using MOCVD for CdTe solar cells, Thin Solid Films 515 (2007) 5808-5813.

26. T. A. Gessert, W. K. Metzger, P. Dippo, S. E. Asher, R. G. Dhere and M. R. Young, Dependence of carrier lifetime on Cu-contacting temperature and

ZnTe:Cu thickness in CdS/CdTe thin film solar cells, Thin Solid Films 517 (2009) 2370-2373.

27. P. N. Gibson, M. A. Baker and M. E. Özsan, Investigation of sulphur diffusion at the CdS/CdTe interface of thin-film solar cells, Surf. Interface Anal. 33 (2002) 825 - 829.

28. The International Centre for Diffraction Data (http://www.icdd.com/); JCPDS files 00-041-1049, 00-049-1302, 00-035-146, 00-010-0434.

29. A. F. Wells, Structural Inorganic Chemistry, Oxford University Press, UK (1984).

30. C. Y. Yeh, Z. W. Lu, S. Froyen, A. Zunger, Zinc-blende–wurtzite polytypism in semiconductors, Phys. Rev. B : Cond. Matter, 46 (1992) 10086 - 10097.

31. B. M. Basol, Processing high efficiency CdTe solar cells, Int. J. Sol. Energy, 12 (1992) 25 - 35.

32. D. Lincot, B. Mokili, M. Froment, R. Cortès, M. C. Bernard, C. Witz, J. Lafait, Phase Transition and Related Phenomena in Chemically Deposited Polycrystalline Cadmium Sulfide Thin Films, J. Phys. Chem. B, 101 (1997), 2174 - 2181.

33. S. B. Quadri, E. F. Skelton, D. Hsu, A.D. Dinsmore, J. Yang, H. F. Gray, B. R. Ratna, Size-induced transition-temperature reduction in nanoparticles of ZnS, Physical review B : Cond. Matter Mater. Phys., 60 (1999) 9191 - 9193.

34. The International Centre for Diffraction Data (http://www.icdd.com/); JCPDS file 00-015-0770.

35. B.E.McCandless, L.V.Moulton, R.W.Birkmire *Progress in Photovoltaics Research* **5** (1997) 249-260

36. N. Amin, K. Sopian and M. Konagai, Numerical modeling of CdS/CdTe and CdS/CdTe/ZnTe solar cells as a function of CdTe thickness, Sol. Energy Mater. Sol. Cells 91 (2007) 1202 - 1208.

37. W. Xia, J.A. Welt, H. Lin, H.N. Wu, M.H. Ho and C.W. Tang, Fabrication of $Cd_{1-x}Zn_xS$ films with controllable zinc doping using a vapor zinc chloride treatment, Sol. Energy Mater. Sol. Cells 94 (2010) 2113 - 2118.

38. Y.Yang, A.Zalar and E.J.Mittemeijer, Depth dependences of the ion bombardment induced roughness and of the interdiffusion coefficient for Si/Al multilayers, Appl. Surf. Sci. 222 (2004) 171 – 179.

39. T. L. Chu, S. S. Chu, J. Britt, C. Ferekides and C. Q. Wu, Cadmium zinc sulfide films and heterojunctions, J. Appl. Phys. 70 (1991) 2688 - 2693.